

Supplementary information for

Facile Patterning of Hierarchical Ionic Microstructures for Pressure-Sensitive Ionic Capacitive Interface

Jiahong Yang^{1,2}, Yao Xiong^{1,2}, Yang Liu^{1,2}, Rui Gu^{1,2}, Shishuo Wu^{1,2}, Chao Liu^{1,2}, Zhong Lin Wang^{1,3,*}, Qijun Sun^{1,2,4,*}

¹ Beijing Institute of Nanoenergy and Nanosystems, Chinese Academy of Sciences, Beijing 101400, P. R. China

² School of Nanoscience and Technology, University of Chinese Academy of Sciences, Beijing 100049, P. R. China

³ Georgia Institute of Technology, Atlanta GA 30332, USA

⁴ Shandong Zhongke Naneng Energy Technology Co., Ltd., Dongying, 257061, P. R. China

*Corresponding author. E-mail: sunqijun@binn.cas.cn, zhong.wang@mse.gatech.edu

Supplementary Figures

Equation S1. The effect of skin resistance on sensing electrodes

Equation S2. Extended theoretical model of electrical double layer (EDL) capacitance under mechanical pressure

Fig S1. 3D printer template cutaway view.

Fig S2. Schematic representation of the process of forming controlled folds in ionic elastomer.

Fig S3. Scanning electron microscope images of the microstructures on the top surface of the sensor electrodes.

Fig S4. Scanning electron microscope images of the microstructures on the top surface of the sensing capacitive electrode (SCE) with a height of 0.8 mm.

Fig S5. Local and global finite element analysis results of quadrangular pyramid microstructure, hierarchical ionic microstructure (HIM), and cylindrical microstructure.

Fig S6. Pressure sensing characteristics of the 0.4 mm high SCE.

Fig S7. Pressure sensing characteristics of the 0.6 mm high SCE.

Fig S8. Pressure sensing characteristics of the 0.8 mm high SCE.

Fig S9. Pressure sensing characteristics of the 1.0 mm high SCE.

Fig S10. Schematic diagram of HISHE films with different ionic liquid contents.

Fig S11. Normalized variation of capacitance with pressure for pressure-sensitive ionic capacitive interface (PSICI) with different ionic liquid contents measured at 5×10^4 Hz.

Fig S12. Capacitive response time of PSICI.

Fig S13. Average initial capacitance magnitude at different time periods, where 30 min of exercise was performed at 2, 4, and 6 hours each after wearing the PSICI.

Fig S14. Schematic of SCE three different substrates (PET, perforated PET, silk) for wear; (b) Plot of capacitance change per hour of compression not measured during 10 hours of wear, where the compression pressure was between 5 ± 1 N.

Fig S15. Physical test diagram for the PSICI array.

Fig S16. Normalized capacitance curves of PSICI pulses corrected for wrist motion.

Fig S17. Capacitive response of hand PSICI sensors.

Table S1. Different parameters comparison between our work and the literature reported flexible capacitive pressure sensors.

Equation S1. The effect of skin resistance on sensing electrodes

Under low-frequency testing conditions (typical frequency $f = 1 \text{ kHz}$, excitation voltage $V_{in} = 1 \text{ V}$), the sensor network is composed of skin resistance¹ $R_{skin} \approx 10 \text{ k}\Omega$ and pressure-sensitive capacitance $C_{sense} \approx 10 \text{ pF} \sim 500 \text{ pF}$, in series. According to the equivalent circuit model^{2,3}, the total impedance is:

$$Z_{total} = R_{skin} + \frac{1}{j\omega C_{sense}},$$

where $\omega = 2\pi f$, and the magnitude of the capacitive reactance $X_C = \frac{1}{\omega C_{sense}}$ relative to the resistance R_{skin} determines the practical measurement error. For instance, when $C_{sense} = 10 \text{ pF}$, the capacitive reactance is:

$$X_C = \frac{1}{2\pi \cdot 10^3 \cdot 10^{-11}} \approx 15.9 \text{ M}\Omega,$$

resulting in a ratio $\frac{X_C}{R_{skin}} \approx 1590$. Here, the contribution of the resistive component to the total impedance is only about 0.063%. For $C_{sense} = 500$:

$$X_C = \frac{1}{2\pi \cdot 10^3 \cdot 5 \times 10^{-10}} \approx 318 \text{ k}\Omega,$$

with $\frac{X_C}{R_{skin}} \approx 31.8$, leading to a resistive contribution of approximately 3.14%.

Analyzing the voltage division effect across the sensing capacitor, the actual voltage applied is:

$$V_{sense} = V_{in} \cdot \frac{X_C}{\sqrt{R_{skin}^2 + X_C^2}}$$

The relative error in capacitance measurement can be approximated as:

$$\text{Error} \approx \frac{R_{skin}}{\sqrt{R_{skin}^2 + X_C^2}} \cdot 100\% \quad (\text{S1})$$

For $C_{sense} = 10 \text{ pF}$, the error is approximately 0.063%, while for $C_{sense} = 500 \text{ pF}$, the error increases to 3.14%. The error trend shows that when $C_{sense} \leq 100 \text{ pF}$, the error

remains below 1%, and even at $C_{\text{sense}} = 200 \text{ pF}$, the error stays under 5%, which aligns with typical sensor tolerance specifications.

In conclusion, under the conditions of $R_{\text{skin}} = 10 \text{ k}\Omega$, $C_{\text{sense}} = 10 \text{ pF} \sim 500 \text{ pF}$, and $f = 1 \text{ kHz}$, the influence of skin resistance on capacitance sensing is dominated by capacitive reactance, with an error range of 0.06%~3.14%. This result confirms that the impact of skin resistance is negligible in practical applications, demonstrating the robustness of the PSICI measurement system.

Equation S2. Extended Theoretical Model of EDL Capacitance under Mechanical Pressure

The initial model of the electrical double layer (EDL) capacitance under equilibrium conditions is derived from the Gouy-Chapman-Stern theory^{4,5}, expressed as:

$$C_{\text{EDL0}} = \left(\frac{1}{C_{H0}} + \frac{1}{C_{GC0}} \right)^{-1}$$

where:

- $C_{H0} = \epsilon_H / \delta_{H0}$ represents the initial Stern layer capacitance, with ϵ_H as the dielectric constant of the Stern layer and δ_{H0} as the initial thickness of the Stern layer.

- $C_{GC0} = \epsilon_r \epsilon_0 / \lambda_{D0}$ denotes the initial Gouy-Chapman diffuse layer capacitance, where ϵ_r is the relative permittivity of the electrolyte, ϵ_0 is the vacuum permittivity, and $\lambda_{D0} = \sqrt{\epsilon_r \epsilon_0 k_B T / (2z^2 e^2 n_0)}$ is the Debye screening length at equilibrium⁶. Here, k_B is the Boltzmann constant, T is the temperature, z is the ion valence, e is the elementary charge, and n_0 is the initial ion concentration.^{7,8}

Under external pressure (P), the Stern layer thickness is compressed as:

$$\delta_H(P) = \delta_{H0}(1 - \beta P)$$

where $\beta(Pa^{-1})$ is the compression coefficient of the Stern layer. Concurrently, the local ion concentration increases due to pressure-induced ion enrichment can be described as:

$$n(P) = n_0(1 + \gamma P)$$

with $\gamma(Pa^{-1})$ defined as the ion enrichment coefficient. This modifies the Debye length to:

$$\lambda_D(P) = \lambda_{D0} \left(1 - \frac{\gamma P}{2} \right)$$

The updated EDL capacitance under pressure is then:

$$C_{\text{EDL}}(P) = \left(\frac{\delta_H(P)}{\epsilon_H} + \frac{\lambda_D(P)}{\epsilon_r \epsilon_0} \right)^{-1}$$

To account for the pressure-dependent contact area in microstructured electrodes, an additional term is introduced:

$$A(P) = A_0(1 + \kappa P),$$

where A_0 is the initial contact area and $\kappa(Pa^{-1})$ the area compression coefficient of the microstructure. The total capacitance becomes:

$$C_{\text{EDL}}(P) = \left(\frac{\delta_H(P)}{\varepsilon_H} + \frac{\lambda_D(P)}{\varepsilon_r \varepsilon_0} \right)^{-1} \cdot \frac{A(P)}{A_0}$$

At high pressures, nonlinear saturation effects emerge. Ion concentration saturation is modeled as:

$$n(P) = n_0 \frac{1 + \gamma P}{1 + \alpha \gamma P},$$

where α (dimensionless) is the ion migration saturation factor. Material hardening effects are described by exponential decay models:

$$\beta(P) = \beta_0 e^{-\eta P}, \quad \kappa(P) = \kappa_0 e^{-\zeta P}$$

with η and $\zeta (Pa^{-1})$ representing the hardening rates of the Stern layer and microstructure, respectively. The comprehensive sensitivity coefficient (S_{total}) integrates these mechanisms:

$$S_{\text{total}} = \kappa_0 + \left(\frac{C_{\text{EDL}0}^2 \beta_0}{C_{H0}^2} + \frac{C_{\text{EDL}0}^2 \gamma}{2C_{GC0}^2} \right) - (\alpha \gamma + \eta + \zeta) \quad (\text{S2})$$

Here:

- κ_0 corresponds to the contact area gain from microstructural deformation.
- The second term combines contributions from Stern layer compression (β_0) and ion enrichment (γ).
- The third term ($\alpha \gamma + \eta + \zeta$) encapsulates inhibition from ion migration saturation (α) and material hardening (η, ζ).

In the low-pressure regime ($P \rightarrow 0$), capacitance response is dominated by synergistic contributions from microstructural deformation ($\kappa_0 P$) and electrochemical mechanisms

(Stern layer compression ($\beta_0 P$) and ion enrichment (γP)). As pressure increases to the moderate-pressure regime ($P \sim 1/\gamma$), ion migration saturation ($\alpha \gamma P \sim 1$) reduces the Debye length shortening rate, while material hardening ($\eta P, \zeta P$) gradually diminishes the efficiency of Stern layer compression and contact area expansion. In the high-pressure regime ($P \gg 1/\gamma$), ion concentration saturates ($n_0 \rightarrow n_0/\alpha$), and microstructural compaction ($\kappa \rightarrow 0$) halts contact area growth, leading to a plateau in capacitance response.

This model establishes a theoretical framework to interpret the experimentally observed multi-regime sensing curves and sensitivity characteristics in EDL-based capacitive pressure sensors. By decomposing the sensitivity coefficient into distinct components, this framework quantitatively links the macroscopic capacitive response to physical mechanisms at both mesoscopic (microstructural deformation) and microscopic (ion

rearrangement, molecular chain compression) scales. It should be emphasized that the theoretical framework is derived from empirical observations of pressure-capacitance nonlinearity, and its quantitative accuracy requires further validation through refined experimental techniques, such as *in situ* interfacial characterization and pressure-dependent dielectric constant measurements. Future studies could compare model predictions with experimental data across diverse microstructural designs and electrolyte systems to systematically improve parameter calibration methods and optimize dynamic response properties of sensors.

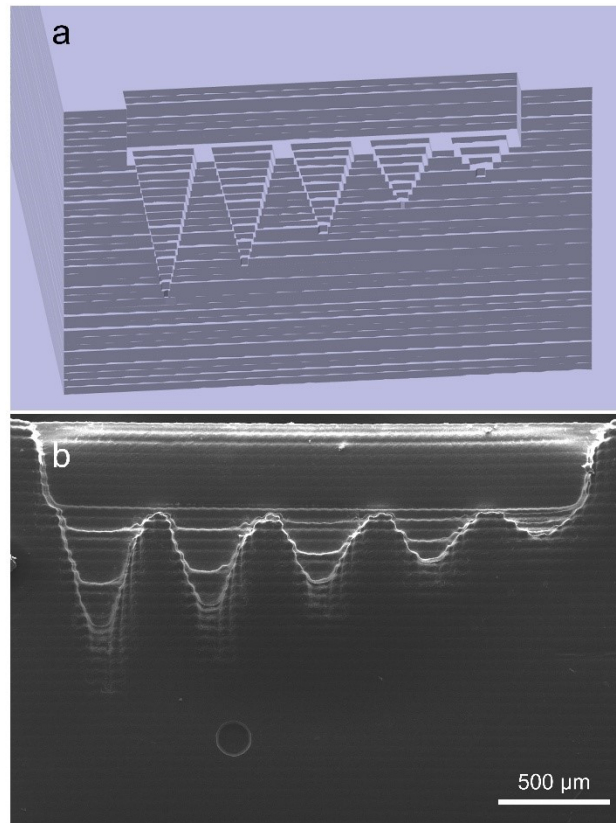


Fig S1. 3D printer template cutaway view. (a) Screenshot of FLASHFORGE's 3D printer slicing software. (b) Electron microscope image of the 3D printed feeler surface after gold spraying.

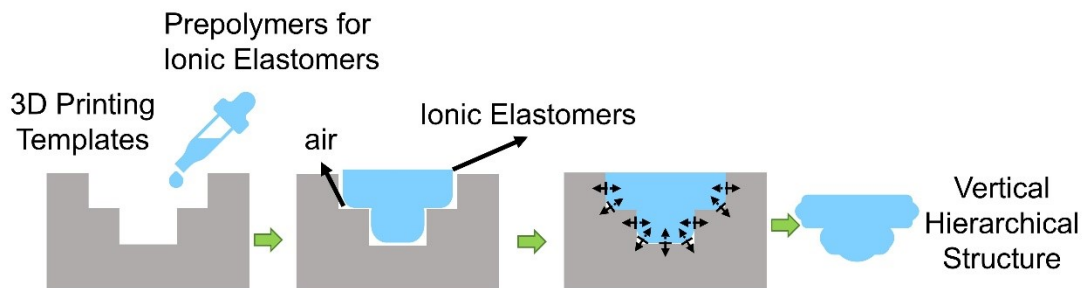


Fig S2. Schematic representation of the process of forming controlled folds in ionic elastomer.

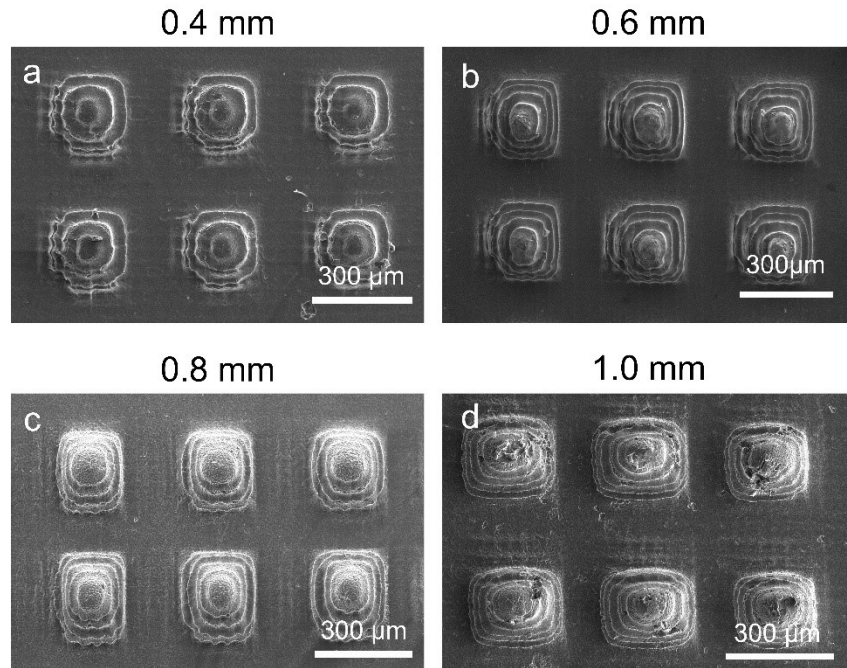


Fig S3. Scanning electron microscope images of the microstructures on the top surface of the sensor electrodes. (a) 0.4 mm height, (b) 0.6 mm height, (c) 0.8 mm height, (d) 1.0 mm height.

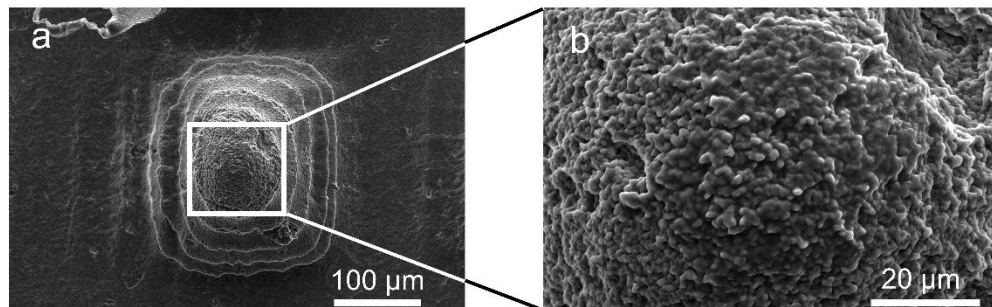


Fig S4. Scanning electron microscope images of the microstructures on the top surface of the SCE with a height of 0.8 mm. (a) Single spike, scale bar 100 μm . (b) Magnified view, scale bar 20 μm .

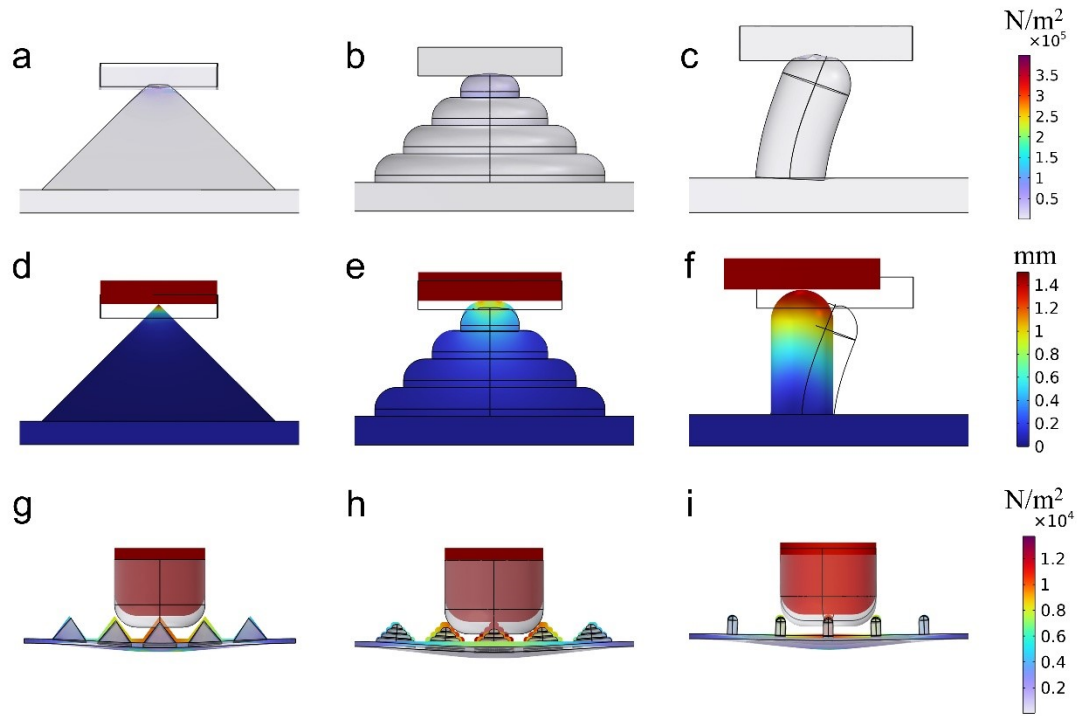


Fig S5. Local and global finite element analysis results of quadrangular pyramid microstructure, HIM, and cylindrical microstructure. (a-c) Internal strain distribution (von Mises stress) with color scale ranging from 0 to 3.5×10^5 N/m²; (d-f) Micro-deformation diagrams with color scale indicating axial displacement (0-1.4 mm); (g-i) Global strain distribution with color scale ranging from 0 to 1.2×10^4 N/m².

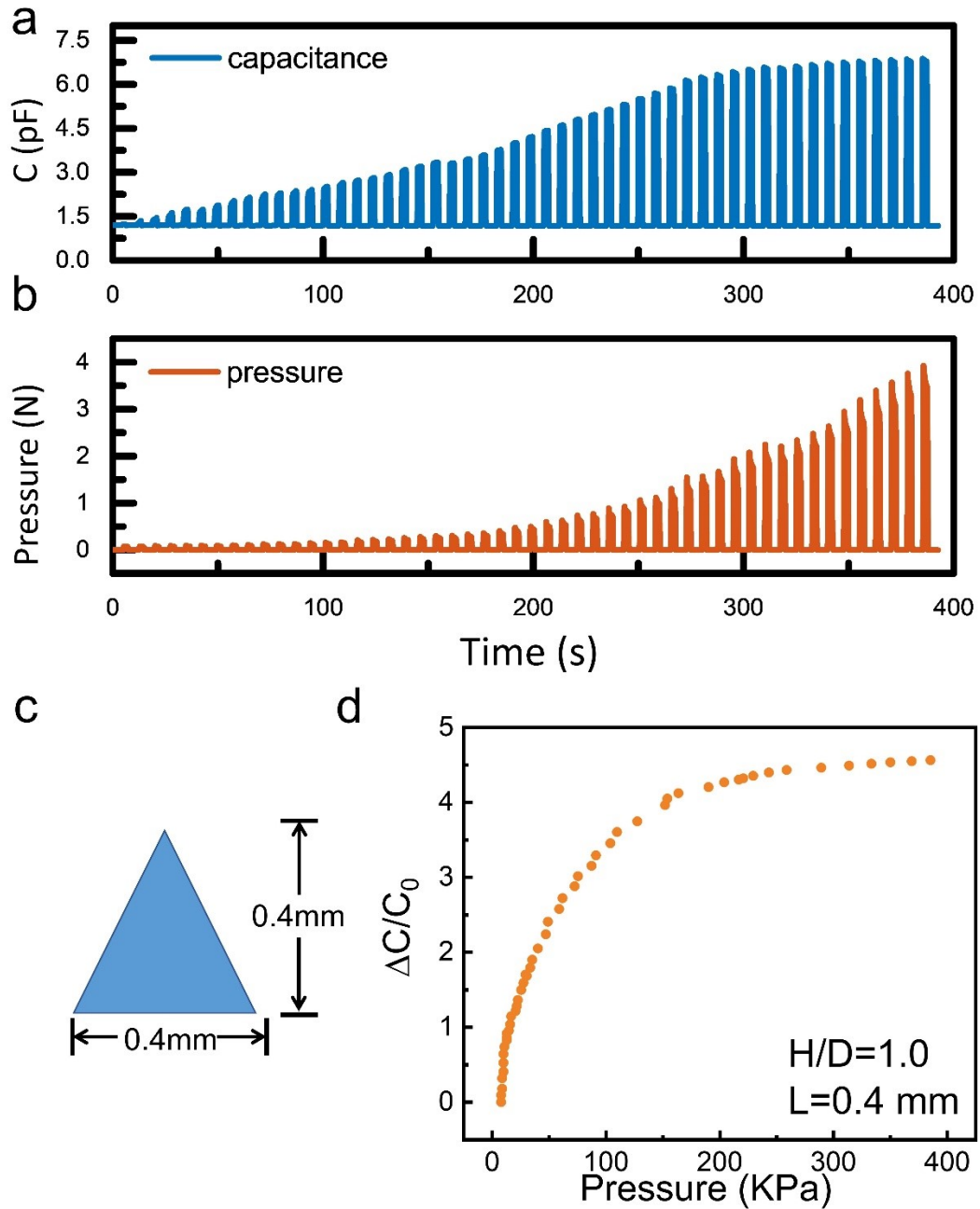


Fig S6. Pressure sensing characteristics of the 0.4 mm high SCE. (a, b) Real-time tip pressure variation graphs and capacitance variation graphs of 0.4 mm height layered pyramidal microstructures. (c) Schematic dimensions of a single 0.4 mm height layered pyramid microstructure. (d) Peak capacitance change-pressure variation plots of layered pyramidal microstructures of 0.4 mm height.

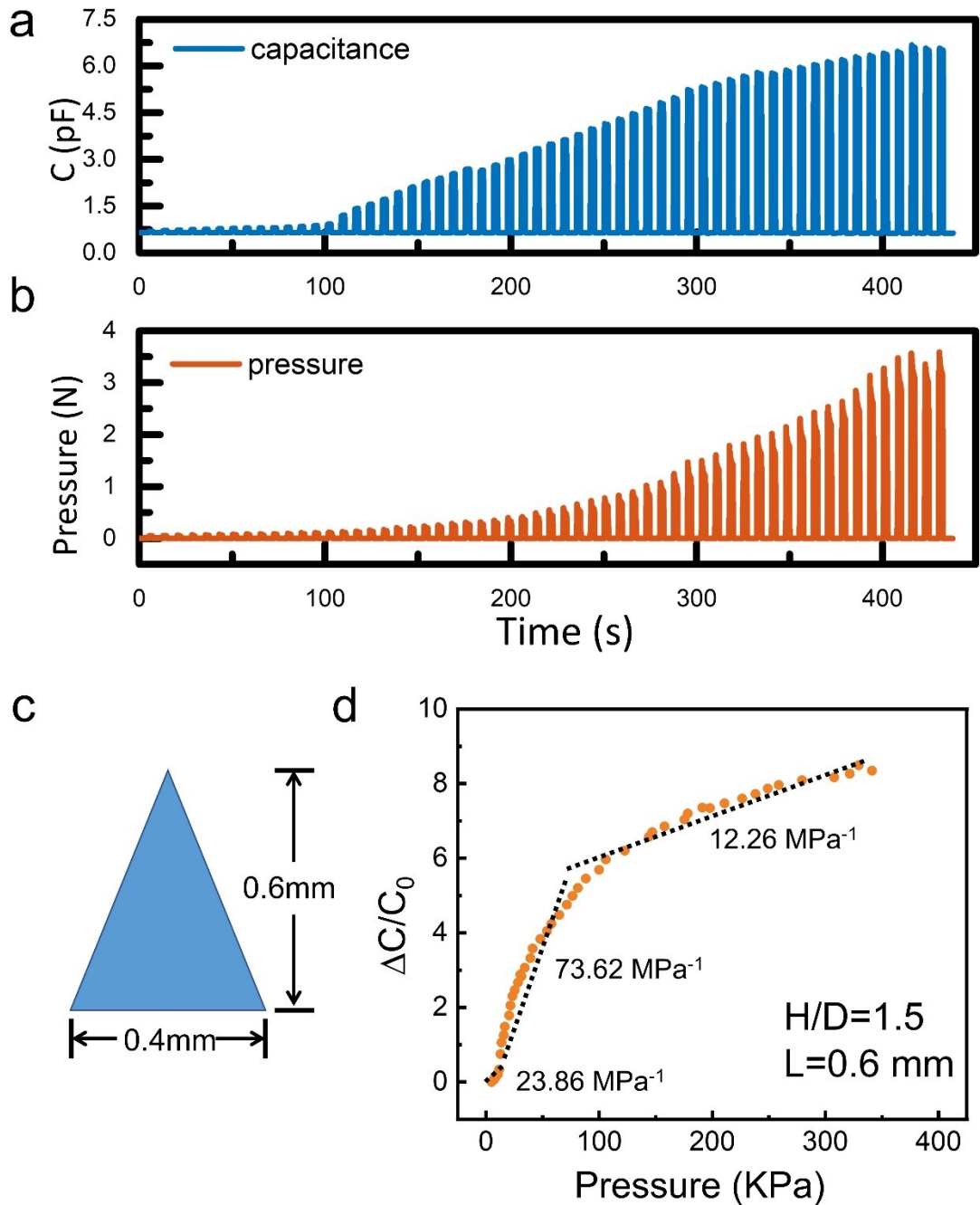


Fig S7. Pressure sensing characteristics of the 0.6 mm high SCE. (a, b) Real-time tip pressure variation graphs and capacitance variation graphs of 0.6 mm height layered pyramidal microstructures. (c) Schematic dimensions of a single 0.6 mm height layered pyramid microstructure. (d) Peak capacitance change-pressure variation plots of layered pyramidal microstructures of 0.6 mm height.

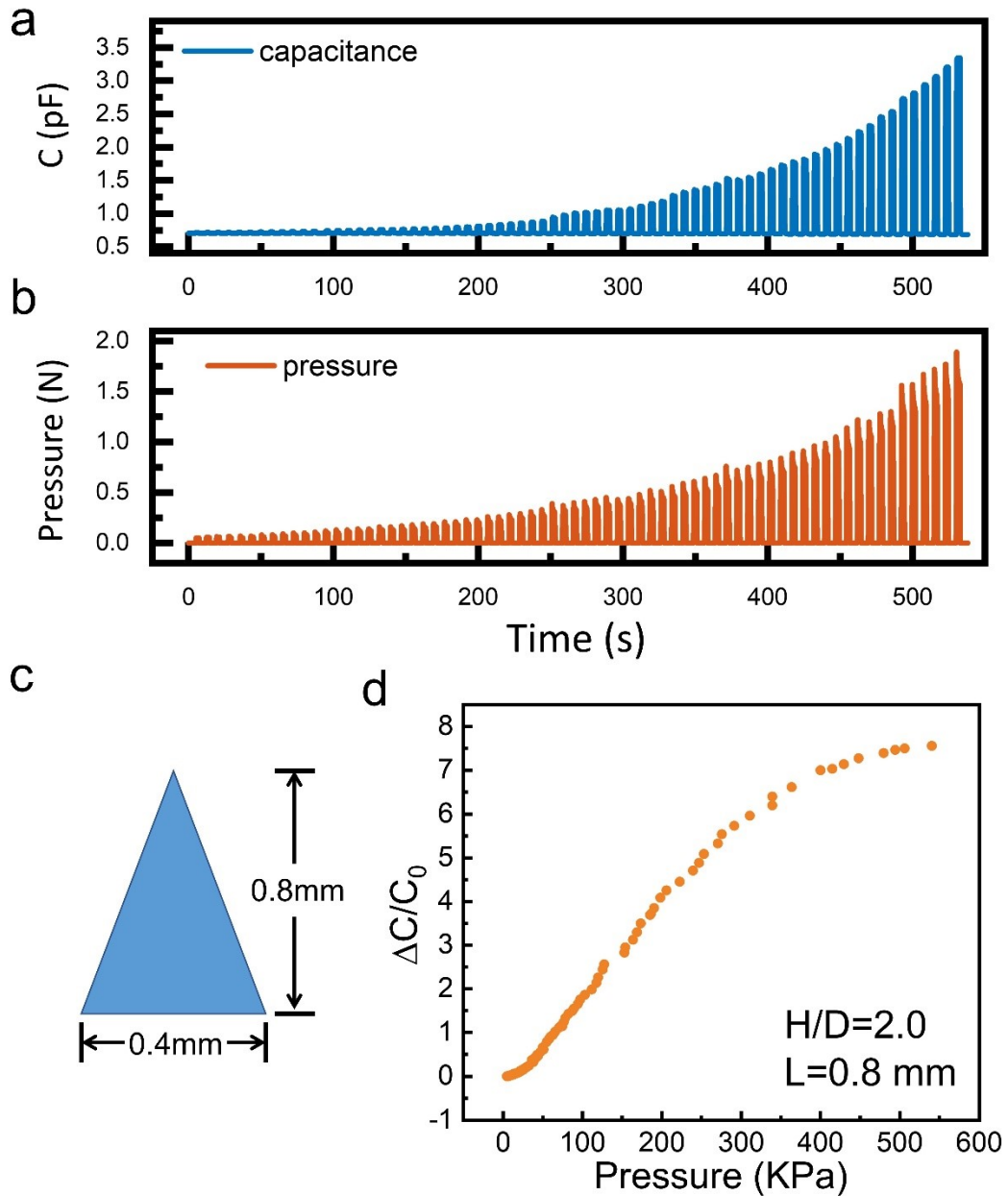


Fig S8. Pressure sensing characteristics of the 0.8 mm high SCE. (a, b) Real-time tip pressure variation graphs and capacitance variation graphs of 0.8 mm height layered pyramidal microstructures. (c) Schematic dimensions of a single 0.8 mm height layered pyramid microstructure. (d) Peak capacitance change-pressure variation plots of layered pyramidal microstructures of 0.8 mm height.

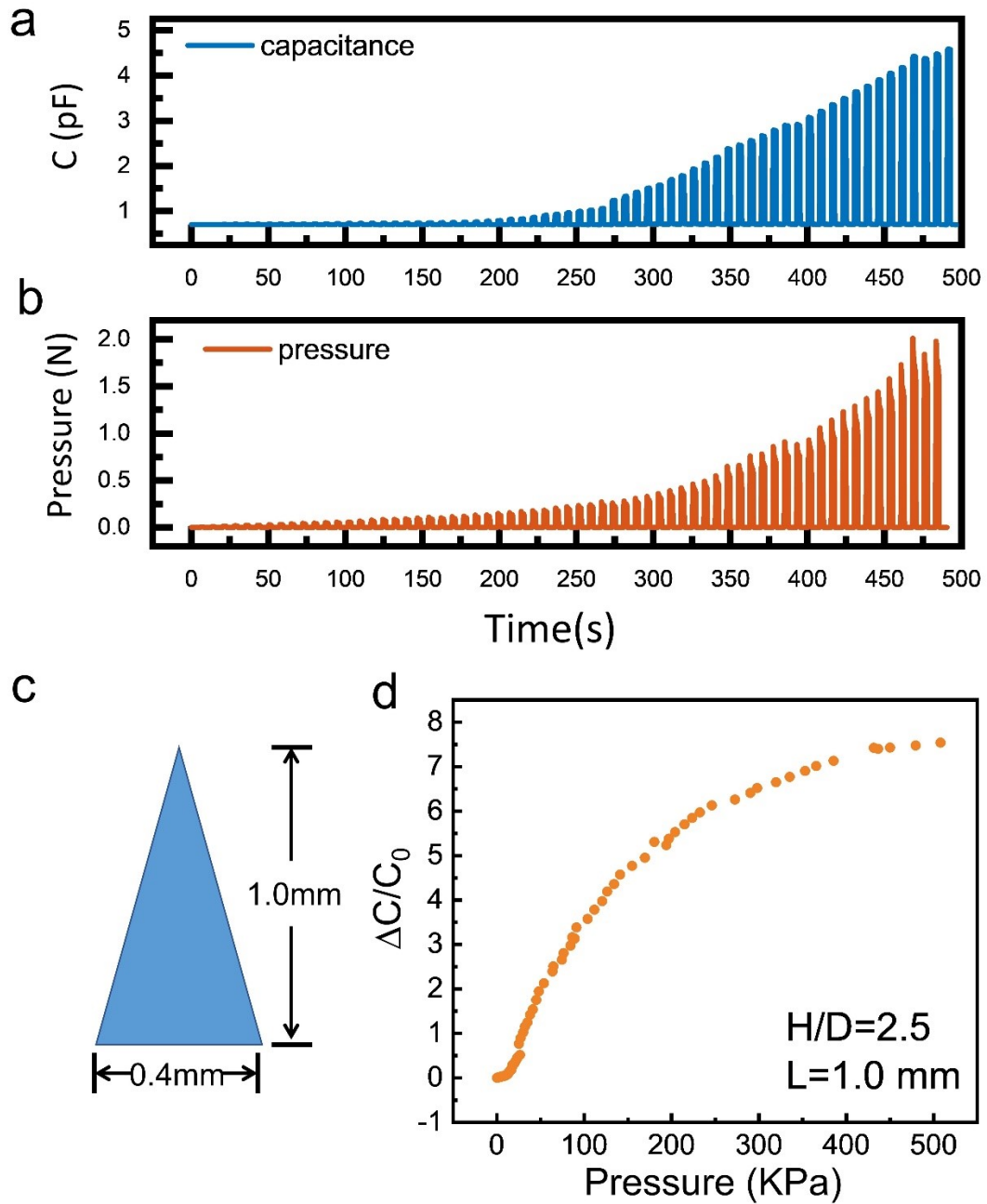


Fig S9. Pressure sensing characteristics of the 1.0 mm high SCE. (a, b) Real-time tip pressure variation graphs and capacitance variation graphs of 1.0 mm height layered pyramidal microstructures. (c) Schematic dimensions of a single 1.0 mm height layered pyramid microstructure. (d) Peak capacitance change-pressure variation plots of layered pyramidal microstructures of 1.0 mm height.

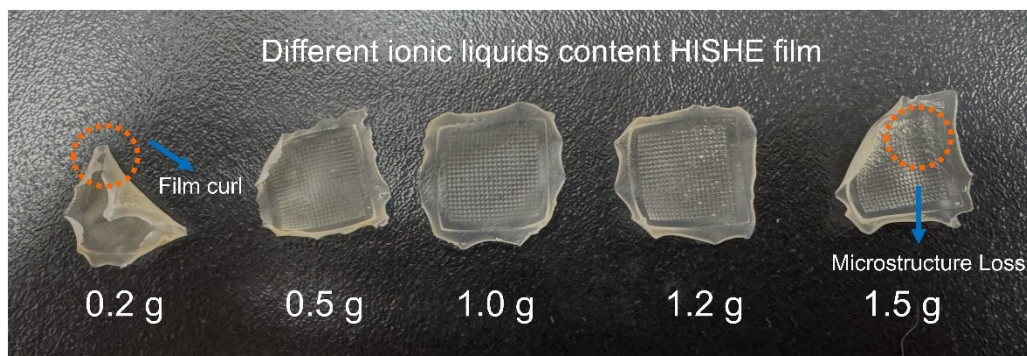


Fig S10. Schematic diagram of HISHE films with different ionic liquid contents.

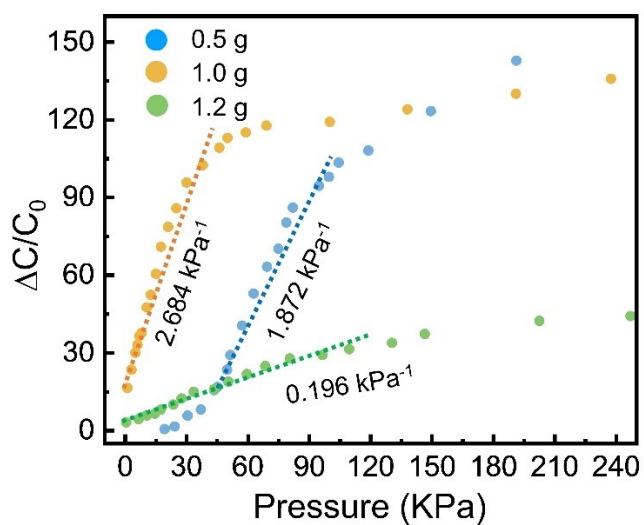


Fig S11. Normalized variation of capacitance with 1 cm² plane pressure for PSICI with different ionic liquid contents measured at 5×10^4 Hz.

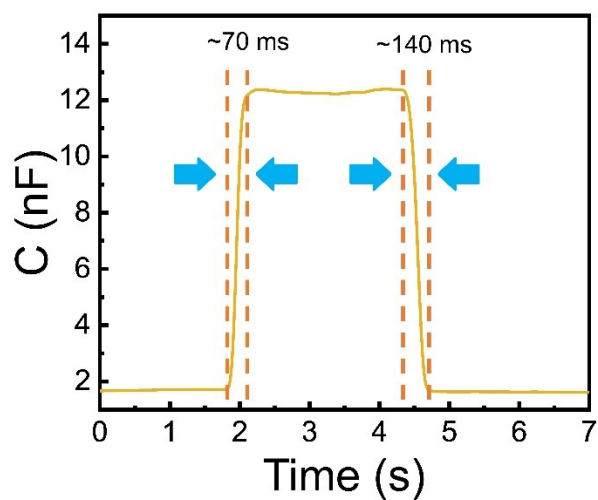


Fig S12. Capacitive response time of PSICI. PSICI Pressure Sensor Sensor capacitive response time plots for pressurization and depressurization at 200 kPa.

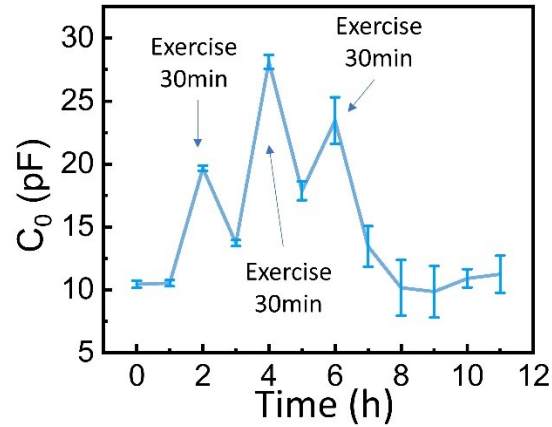


Fig S13. Average initial capacitance magnitude at different time periods, where 30 min of exercise was performed at 2, 4, and 6 hours each after wearing the PSICI.

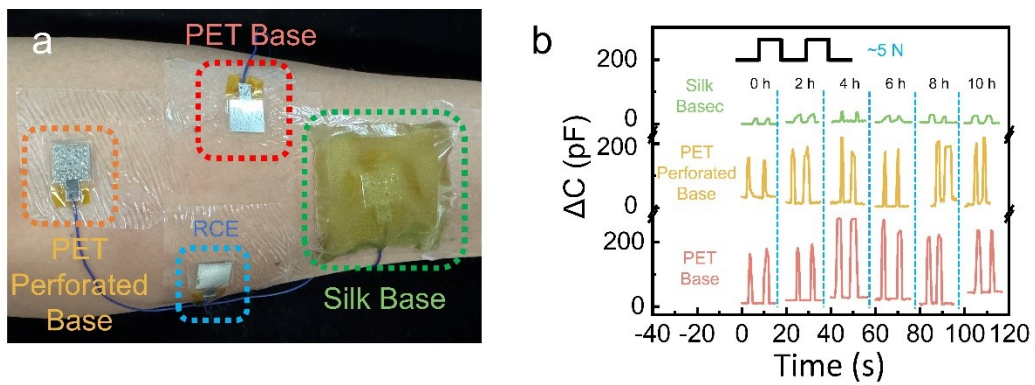


Fig S14. Schematic of SCE three different substrates (PET, perforated PET, silk) for wear; (b) Plot of capacitance change per hour of compression not measured during 10 hours of wear, where the compression pressure was between 5 ± 1 N.

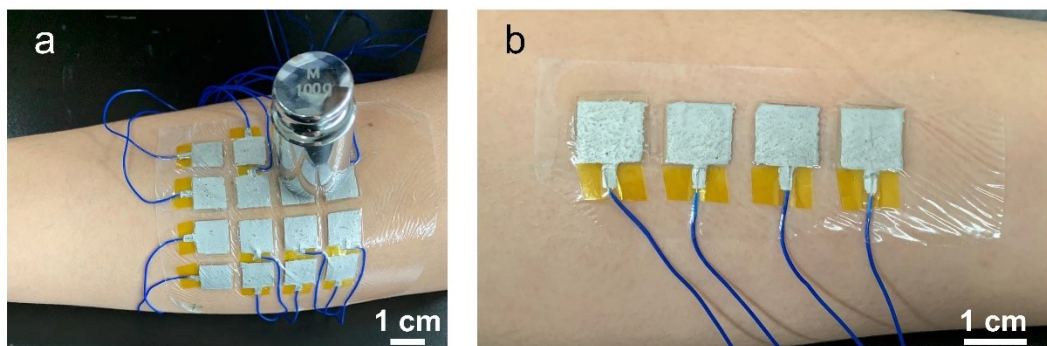


Fig S15. PSICI Array Physical Test Diagram. (a) Photograph of the PSICI 4×4 array and photograph of the placement of the weights. (b) Photograph of the PSICI 1×4 array on the arm.

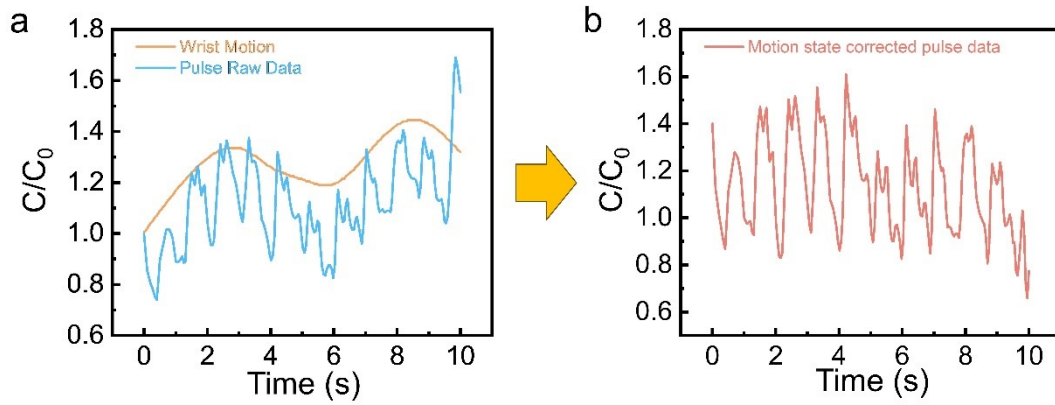


Fig S16. Normalized Capacitance Curves of PSICI Pulses Corrected for Wrist Motion. (a) Normalized capacitance change of pulse and wrist motion detected by RCE of the wrist PSICI in the motion state. (b) PSICI pulse normalized capacitance curve corrected for wrist motion.

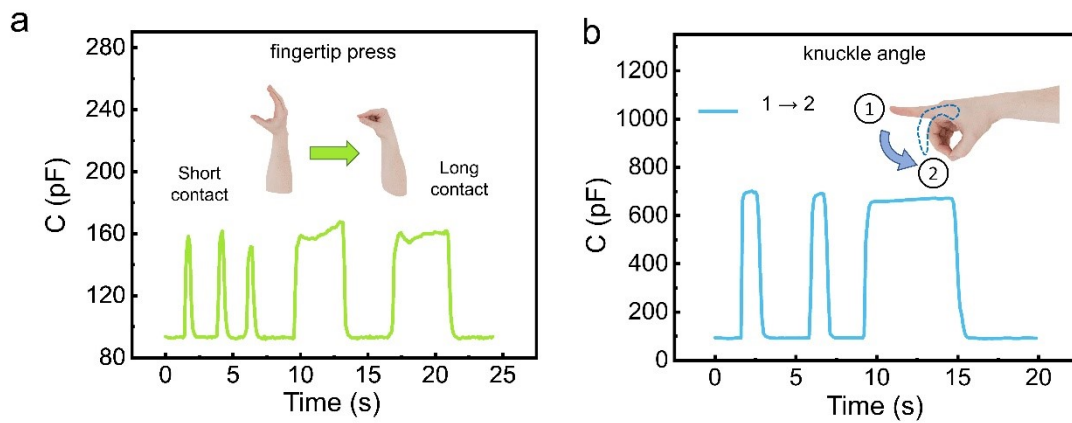


Fig S17. Capacitive Response of Hand PSICI Sensors. (a) Capacitive response of fingertip contact with PSICI sensor. (b) Capacitive response of finger knuckle folding/unfolding with PSICI sensor.

Table S1. Different parameters comparison between our work and the literature reported flexible capacitive pressure sensors.

Sensing structure and method	Pressure Range	Optimal Sensitivity	Response time	Cycling stability	Ref
Dual-Electrode Capacitor Interface	0-400 kPa	2.648 kPa ⁻¹	70/140 ms	5,000	This work
Sandwich Microstructure Capacitors	0–280 kPa	0.75 kPa ⁻¹ (0-2 kPa)	80 ms	24,000	9
Sandwich Microstructure Capacitors	1500 kPa	0.0012 kPa ⁻¹ (linear range)	166.9/199 ms	33,000	10
Fiber Resistive-Capacitive Sensors	0-22.7 kPa	1.2 kPa ⁻¹ (0–2 kPa)	~20 ms	2,500	11
Sandwich Microstructure Capacitors	130 kPa	0.12 kPa ⁻¹ (linear range)	46 ms	3,000	12
Sandwich Microstructure Capacitors	70 Pa–800 kPa	17 MPa ⁻¹	300 ms	1,000	13
Multilayer Sandwich Microstructure Capacitors	0–2 kPa	0.28 kPa ⁻¹	65/78 ms	1,000	14
Capacitive Dual-Electrode Pair Sensor	0-1122.5 kPa	0.0012 kPa ⁻¹	166.9/199 ms	33,000	15
Sandwich Microstructure Capacitors	0-300 kPa	0.018 kPa ⁻¹ (0-150 kPa)	46.8 ms	100,000	16
Sandwich Microstructure Capacitors	0-550 kPa	46.6 MPa ⁻¹	94/97 ms	11,400	17
Multilayer Sandwich Microstructure Capacitors	0–800 kPa	0.784 kPa ⁻¹ (< 80 kPa)	30/50 ms	10,000	18

References

1. K. Ehtiati, J. Eiler, A. Bochynska, L. L. Nissen, E. Strøbech, L. F. Nielsen and E. Thormann, *ACS Applied Bio Materials*, 2023, 6, 3033-3051.
2. B. Ramezanzadeh, S. Niroumandrad, A. Ahmadi, M. Mahdavian and M. H. M. Moghadam, *Corrosion Science*, 2016, 103, 283-304.
3. S. Wang, M. Yan, Y. Li, C. Vinado and J. Yang, *Journal of Power Sources*, 2018, 393, 75-82.
4. K. B. Oldham, *Journal of Electroanalytical Chemistry*, 2008, 613, 131-138.
5. J. Wu, *Chemical Reviews*, 2022, 122, 10821-10859.
6. S. Prakash and J. Yeom, in *Nanofluidics and Microfluidics*, eds. S. Prakash and J. Yeom, William Andrew Publishing, 2014, DOI: <https://doi.org/10.1016/B978-1-4377-4469-9.00002-0>, pp. 9-38.
7. D.-e. Jiang, D. Meng and J. Wu, *Chemical Physics Letters*, 2011, 504, 153-158.
8. K. Kiyohara and K. Asaka, *The Journal of Physical Chemistry C*, 2007, 111, 15903-15909.
9. W. Hong, X. Guo, T. Zhang, A. Zhang, Z. Yan, X. Zhang, X. Li, Y. Guan, D. Liao, H. Lu, H. Liu, J. Hu, Y. Niu, Q. Hong and Y. Zhao, *ACS Applied Materials & Interfaces*, 2023, 15, 46347-46356.
10. R. Han, Y. Liu, Y. Mo, H. Xu, Z. Yang, R. Bao and C. Pan, *Advanced*

Functional Materials, 2023, 33, 2305531.

11. X. Qu, J. Li, Z. Han, Q. Liang, Z. Zhou, R. Xie, H. Wang and S. Chen, ACS Nano, 2023, 17, 14904-14915.
12. L. Wu, X. Li, J. Choi, Z.-J. Zhao, L. Qian, B. Yu and I. Park, Advanced Functional Materials, 2024, 34, 2312370.
13. Y. Chen, Z. Huang, F. Hu, J. Peng, T. Huang, X. Liu, C. Luo, L. Xu and K. Yue, ACS Applied Materials & Interfaces, 2023, 15, 58700-58710.
14. R. Li, M. Panahi-Sarmad, T. Chen, A. Wang, R. Xu and X. Xiao, ACS Applied Electronic Materials, 2022, 4, 469-477.
15. Y. Chen, T. Feng, C. Li and F. Qin, Small, 2024, 20, 2406739.
16. J.-S. Yang, M.-K. Chung, J.-Y. Yoo, M.-U. Kim, B.-J. Kim, M.-S. Jo, S.-H. Kim and J.-B. Yoon, Nature Communications, 2025, 16, 2024.
17. M. Farman, Surendra, R. Prajesh, A. K. Upadhyay, P. Kumar and E. Thouti, ACS Applied Materials & Interfaces, 2023, 15, 34195-34205.
18. M. Wang, Z. Lin, S. Ma, Y. Yu, B. Chen, Y. Liang and L. Ren, Advanced Healthcare Materials, 2023, 12, 2301005.